HHS Public Access

Author manuscript

J Phys Chem Lett. Author manuscript; available in PMC 2019 January 04.

Published in final edited form as:

J Phys Chem Lett. 2018 June 07; 9(11): 2886–2892. doi:10.1021/acs.jpclett.8b01191.

In Situ Identification of Nanoparticle Structural Information Using Optical Microscopy

Kayla S.B. Culver[a], **Tingting Liu**[b], **Alexander J. Hryn**[a], **Ning Fang**[c], and **Teri W. Odom**[a,b,*]

[a]Department of Materials Science and Engineering, Northwestern University, Evanston, IL 60208, USA

[b]Department of Chemistry, Northwestern University, Evanston, IL 60208, USA

[c]Department of Chemistry, Georgia State University, Atlanta, GA 30302, USA

Abstract

Diffraction-limited optical microscopy lacks the resolution to characterize directly nanoscale features of single nanoparticles. This paper describes how structural features of gold nanostars can be identified using differential interference contrast (DIC) microscopy. First, we established structure-property relationships between categories of nanoparticle shapes and DIC optical images and then validated the correlation with electrodynamic simulations and electron microscopy. We found that DIC image patterns of single nanostars could be differentiated between 2D and 3D geometries. DIC images were also used to distinguish asymmetric and 4-fold symmetric structures and track nanoparticle orientation. Finally, we demonstrated how this wide-field optical technique can be used for *in situ* characterization of single nanoparticles rotating at a glass-water interface.

TOC GRAPHIC

*Corresponding Author todom@northwestern.edu.

Supporting Information. The following files are available free of charge.

Additional methods for FDTD simulated DIC images; scheme of DIC optical components and generation of contrast; TEM images of AuNS; AuNS feature sizes; ensemble optical properties of AuNS; simulated electric field profiles; image processing details; characterization of other 2D and 3D AuNS; characterization of spherical Au NPs; simulated 4-fold symmetric 3D AuNS; high temporal resolution orientation tracking of 2D and 3D AuNS; details on correlation between EM and optical microscopy (PDF)

Wide-field video of many AuNS rotating at glass-water interface, acquired at 2 fps, playing at 8× real speed (AVI).

Zoomed-in video of 2D (left) and 3D (right) AuNS rotating at glass-water interface, acquired at 2 fps, playing at 8× real speed (AVI).

High temporal resolution zoomed-in video of 2D (left) and 3D (right) AuNS rotating at glass-water interface, acquired at 50 fps, playing at real speed (AVI).

Notes

The authors declare no competing financial interest.

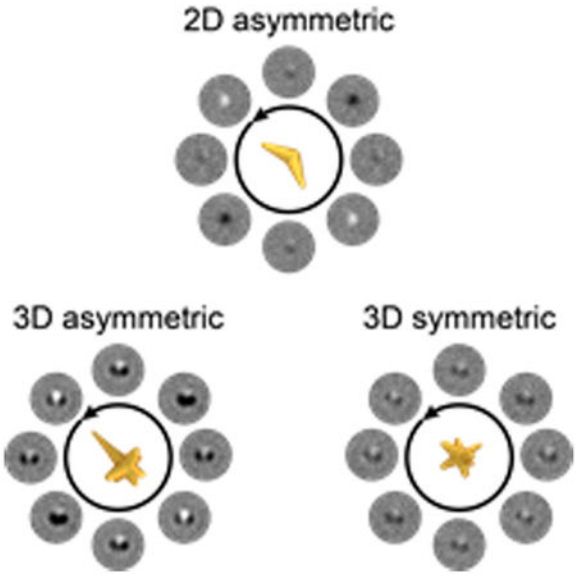

Keywords

differential interference contrast (DIC) microscopy; gold nanostars; in situ nanoparticle characterization; nanoscale structural characterization; orientation; 3D geometry

Nanoparticle (NP) shape is an important parameter for tuning the physical properties of metal nanoparticles.[1-4] Small variations in NP structure can result in large changes in properties such as far-field optical response[4-9] and chemical reactivity.[10-14] Gold nanostars (AuNS) synthesized in Good's buffers are model anisotropic NPs with complex and tailorable 3D geometries because they have sharp-tipped branches that can vary in length, number, and orientation, and their unique overall shape displays multiple types of curvature (positive, negative, neutral).[8-9, 12, 15] Curvature effects of AuNS have been exploited for light-triggered drug release,[16-18] near-infrared imaging,[19] photothermal heating,[8, 19] surface-enhanced Raman spectroscopy,[20] and magnetic resonance imaging contrast agent enhancement.[11-12]

The shape of NPs is typically characterized by electron microscopy (EM) tools because of the resolution required to visualize nanoscale features. Liquid cell EM allows *in situ* imaging of NPs in liquids, but the high energy electron beam can damage or alter the native properties of the sample, and the complicated set-up and small imaging area limit the versatility of this technique.[21] Moreover, although the motion of single NPs can be tracked using standard wide-field optical microscopy methods,[22-29] the NPs appear as diffraction-limited spots, and specific features cannot be resolved. The structural information that has been obtained from optical methods such as differential interference contrast (DIC) and dark-field (DF) microscopy has mostly been limited to the *orientation* of anisotropic NPs.[29-31]

Here we demonstrate how different types of nanoscale structural information can be identified within individual NPs by wide-field optical microscopy. We focus on AuNS as a

model NP system because they can be synthesized with both 3D and 2D (planar) architectures. We show how DIC image patterns combined with electrodynamics simulations can reveal complex structural features from single AuNS, including orientation, symmetry, and overall geometry. Finally, we tested how this analysis method could be used for prospective dynamic and biological studies by *in situ* characterization of AuNS in a liquid environment.

Wide-field optical microscopy of gold nanostars.

In DIC microscopy, elliptically polarized light is split by the first Nomarski prism into two beams—ordinary and extraordinary—that are mutually orthogonal and spatially separated (Figure 1a). In our setup, the polarization directions of the ordinary and extraordinary beams were at ca. 45° and 135° relative to the $+x$ direction of the images, respectively, indicated by white arrows in the DIC images. The two beams undergo independent phase shifts through the sample and are re-combined by the second Nomarski prism to form the final interference-based image (Figure S1). Since the final optical image is produced by small phase shifts and interference, DIC microscopy is advantageous over scattering-based methods such as DF microscopy for imaging small NPs.[32] Au NPs are readily visualized by DIC microscopy when imaged near their localized surface plasmon (LSP) resonance.[33-35]

AuNS were synthesized in a seedless-method by reducing $HAuCl_4$ with HEPES (4-(2-hydroxyethyl)-1-piperazineethanesulfonic acid) according to our previous work.[9, 15, 36-37] Without post-processing by sorting,[12] a variety of complex NP geometries are produced with varying branch length, number, and orientation (Figure S2). AuNS core diameters are 20 – 30 nm, their branch tips taper down to radii of *ca.* 5 nm, and their mean branch length is *ca.* 20 nm (Methods, Figure S3). We used DIC microscopy as the wide-field imaging technique to visualize AuNS since they have relatively small features and overall sizes.

We acquired DIC images using a 700/10-nm bandpass (BP) filter because the center wavelength was near the ensemble AuNS LSP resonance (Figure S4). Figure 1b shows a wide-field DIC image of dispersed AuNS that appear as diffraction-limited bright and/or dark spots. Zoomed-in images highlight the different types of contrast and image patterns produced by single AuNS (Figure 1c). Since different particles produced distinct DIC images, we hypothesized that DIC imaging could provide sub-NP structural information based on variations in contrast and image patterns. To establish how NP geometry is related to DIC image patterns, we correlated the DIC optical images with scanning electron microscopy (SEM) images of the same individual particles.

DIC image patterns can differentiate between 2D and 3D structures.

From a single wide-field DIC image, two distinct types of image patterns were observed for AuNS: (1) bright or dark spots without lobes (Figure 2a) and (2) bright- and dark-lobed structures (Figure 2b). To correlate these image patterns to NP structure, we compared side-by-side DIC images and corresponding SEM images. We found that DIC images without lobe patterns were from 2D planar AuNS with all branches in the same plane (Figure 2a).

Lobed DIC image patterns were present for 3D AuNS that had multiple branches pointing along different 3D directions (Figure 2b).

To understand in more detail how AuNS geometry influences DIC image patterns, we developed a finite-difference time-domain (FDTD) model to simulate DIC images of NPs (Methods). These numerical simulations provide key structural insight because DIC images can be generated for NPs with complex geometries that cannot be described analytically. Similar to experimental results, the simulated 2D AuNS produced DIC images without lobes (Figure 2c), while simulated 3D AuNS produced more complex image patterns with distinct bright and dark lobes (Figure 2d). Lobed patterns in DIC images have previously been observed from Au nanorods tilted with respect to the image plane.[38] These patterns were hypothesized to be a result of asymmetric electric field profiles from the tilted rods interacting with the intermediate DIC beams.[38] Since our simulation model could calculate the electric fields produced by the interaction of NPs with *intermediate* polarized beams in the DIC light path, we tested whether differences in the electric field profiles were responsible for the different DIC image patterns produced by 2D and 3D AuNS. Figure S5 shows the $|\mathbf{E}|^2$ distribution parallel to the image plane, 50 nm above the simulated 2D and 3D AuNS. 2D AuNS with in-plane branches produced intensity profiles that were symmetric and had equal magnitude (Figure S5a). 3D AuNS with out-of-plane branches produced an $|\mathbf{E}|^2$ profile with asymmetry in shape and intensity (Figure S5b). These simulations confirm our hypothesis that lobed DIC image patterns can be attributed to the out-of-plane, 3D geometry of AuNS. We expect our simulation method could be expanded to predict DIC images of other complex shapes and NP assemblies, or to characterize the effects of out-of-plane NP rotation, which is difficult to control experimentally.

Orientation-dependent DIC of 2D nanostars.

DIC imaging has been used to track rotation of Au nanorods because they appear brightest when aligned to one polarization direction and darkest when rotated 90° and aligned to the other.[30, 35, 39] We used SEM to validate the particle alignment relative to the ordinary and extraordinary beams and investigated how AuNS geometry influenced the orientation-dependent DIC images. Figure 3a shows a series of DIC images of a 2D AuNS through a 180° rotation (note: the rotation angle α refers to the angle of the substrate relative to the microscope stage), where features in the DIC images varied from fully bright to fully dark without lobed patterns.

We quantified the DIC contrast, $(I - I_{bkg})/I_{bkg}$, where I is the intensity of the particle signal, and I_{bkg} is the intensity of the background in a defined region surrounding the particle (Methods, Figure S6). These data were fit to $\sin^2(\alpha)$ ($R^2 = 0.98$) to enable quantitative comparisons among particles. For example, we used the amplitude ($A = 0.98 \times 10^{-2}$) (Figure 3b) of the fit as an indication of the magnitude of contrast change with rotation. We also used the maximum and minimum of the fitted data to identify the α at which each particle produced brightest and darkest contrast, respectively. The brightest contrast for this AuNS occurred at substrate angle $\alpha = 65°$ (Figure 3, red box). Analysis of the SEM image at $\alpha = 65°$ showed the AuNS orientation was $\theta = 136°$, where θ is relative to the $+x$ direction of the images, indicating particle alignment with the extraordinary beam (Figure 3b, inset). The

darkest contrast was produced when $\alpha = 155°$ (Figure 3, blue box), which had a 90° rotation and with particle alignment along the ordinary beam.

We analyzed five 2D AuNS with particle-to-particle variations in geometry such as size of core, length and number of branches, and angles between branches (Figure S7). All 2D AuNS produced DIC images without lobes and showed similar orientation-dependent contrast results. The brightest DIC contrast occurred when each 2D AuNS was aligned with the extraordinary beam (average particle orientation $\theta_{mean} = 137 \pm 4°$), and mean amplitude of the contrast fits was $A_{mean} = 1.1 \pm 0.2 \times 10^{-2}$ (Figure S7). Therefore, DIC contrast can be used to consistently identify orientations of 2D AuNS relative to the defined DIC imaging set-up.

Orientation-dependent DIC of 3D nanostars.

Lobed image patterns were produced by all 3D AuNS at all rotation angles, but we observed two classes of orientation-dependent contrast (Figure 4). The images and contrast in Figures 4a-b are representative of the first category, asymmetric 3D AuNS. These DIC image patterns varied from mostly bright with dark lobes to mostly dark with bright lobes. The quantified contrast showed a good fit to $\sin^2(\alpha)$ ($R^2 = 0.98$) and strong orientation-dependent changes in contrast ($A = 1.03 \times 10^{-2}$). We verified that orientation-dependent contrast could be used to identify orientation of asymmetric 3D AuNS by correlating with SEM images (Figure 4c). Four asymmetric 3D AuNS with slight variations in length and spatial distribution of branches were analyzed and showed similar orientation-dependent contrast properties (Figure S8). The brightest DIC contrast occurred when all particles were aligned with the extraordinary beam ($\theta_{mean} = 137 \pm 9°$) and mean amplitude of $\sin^2(\alpha)$ fits was $A_{mean} = 1.0 \pm 0.3 \times 10^{-2}$ (Figure S8). Thus, DIC contrast can identify orientation of both 3D and 2D NPs. The A_{mean} and thus magnitude of contrast change with rotation were also similar between asymmetric 3D and 2D AuNS.

Interestingly, we observed another category of 3D AuNS that showed lobed image patterns that were similar at all rotation angles (Figure 4d). The DIC contrast of the AuNS in Figures 4d-f showed very weak orientation-dependence: the amplitude of the $\sin^2(\alpha)$ fit ($R^2 = 0.85$) was $A = 0.23 \times 10^{-2}$, 4.4× lower than A_{mean} of the other 3D AuNS (Figure S8). Orientation-independent DIC contrast is expected to occur for isotropic particles such as spheres (Figure S9) because they interact equally with both of the light beams. Since the two DIC beams are orthogonally polarized, we hypothesized 4-fold symmetry would also produce orientation-independent contrast. Indeed, this particle was nearly 4-fold symmetric (Figure 4f), where the tip-to-tip lengths and the angle between the two visible sets of branches were approximately 38 nm and 42 nm and 89°. Based on image contrast and pixel resolution, we estimate a resolution of length and angle measurements to be 2–3 nm and 2–4°, respectively. To confirm our assignment, we used our FDTD model to simulate DIC images of a 3D AuNS with 4-fold symmetry in the rotation plane. The simulated DIC images and the quantified contrast were the same at all orientations, confirming that 4-fold symmetric particles produce orientation-independent DIC contrast (Figure S10). Thus, our experimental and theoretical results indicate that orientation-dependent DIC contrast can be used to identify symmetry properties of NPs with complex geometries.

In situ structural characterization of AuNS in a liquid environment.

To demonstrate the use of DIC microscopy for *in situ* characterization with sub-NP resolution in fluids, we recorded AuNS rotating at a glass-water interface (Supporting Movies S1-S2). 150-s videos were streamed using 0.5-s exposure times (2 fps) over a large field-of-view (67 μm × 67 μm). We demonstrated structural characterization and orientation tracking of two classes of AuNS. Notably, we observed the same types of image patterns as those on AuNS fixed on substrates: (1) DIC image patterns without lobes corresponding to 2D AuNS (structure similar to rods), and (2) images with clear lobed patterns suggesting AuNS with asymmetric 3D geometry. Figure 5a shows 21 sequential frames (10.5 s) from the video of a 2D AuNS. The images varied between bright and dark contrast, where the particle rotated on the substrate. We estimated AuNS orientation and tracked rotation by quantifying DIC contrast (Figure 5b). As established in the static studies, the brightest contrast indicated particle alignment with the extraordinary beam (Figures 5a-b, red boxes), and darkest contrast corresponded to alignment with the ordinary beam (Figures 5a-b, blue boxes). Figure 5c shows 21 sequential frames (10.5 s) zoomed-in around a 3D AuNS. The image pattern varied between bright with dark lobes and dark with bright lobes under rotation, indicating that we can distinguish between 2D and 3D nanoscale geometries of NPs in motion. We also quantified the contrast to track orientation of this 3D AuNS under rotation (Figure 5d), which displayed periods of alignment with the polarizations of the extraordinary (red boxes) and ordinary (blue boxes) beams.

Since high temporal resolution is important for accurate analysis of fast NP dynamics, we tested the exposure time limits for orientation tracking of dynamic AuNS. 300-frame videos were streamed over the same 67 μm × 67 μm field-of-view with exposure times down to 0.02 s (50 fps). Supporting movies S3 shows an example of rotating 2D (left) and 3D (right) AuNS acquired at 50 fps. The particles produced sufficient intensity to enable quantification of contrast and thus orientation tracking at this high temporal resolution (Figure S11). Thus, we have demonstrated that DIC microscopy is a promising tool for high temporal resolution tracking of dynamic NPs with a variety of geometries. Additionally, although the NPs in this study remained at a fixed focal plane, DIC microscopy is compatible with 3D tracking methods,[23] which could be adapted to enable NP orientation tracking in environments with z-axis motion such as live cells.

In conclusion, we described new categories of nanoscale structural features that can be identified using wide-field diffraction-limited optical microscopy tools. AuNS were model probes to expand the capabilities of single-particle DIC microscopy because a variety of geometries can be produced simultaneously during synthesis. By correlating DIC microscopy and FDTD simulations and validating by SEM, we demonstrated that AuNS with 3D geometries produced complex lobed DIC image patterns, while 2D particles produced plain image patterns without lobes. Importantly, we used the results of the static correlation study to demonstrate *in situ* structural characterization and high temporal resolution orientation tracking of single AuNS rotating at a glass-water interface. We anticipate that the results of this study could be extended to track orientation of other asymmetric NPs and to categorize NPs of unknown shape as 2D or 3D and symmetric or asymmetric. This method may also be used for high-throughput examination of

microfabricated NP arrays[40-42] or conjugated block co-polymer films.[43-44] Finally, because of the technical advantages of low-light levels, short exposure times, ambient conditions, and wide-field imaging nature, DIC microscopy is promising for applications that require analysis of NP structural information in liquid environments, such as shape-dependent NP interactions with live cells.[27-28, 45]

EXPERIMENTAL METHODS

Sample Preparation for Correlation Study.

All materials were purchased from Sigma Aldrich unless otherwise noted. AuNS were synthesized by reducing $HAuCl_4$ with HEPES buffer (Atlanta Biologicals, pH 7.3. To prepare a 20-mL batch of AuNS, $HAuCl_4$ was added to the HEPES buffer, with the final concentration being 100 mM HEPES and 0.2 mM $HAuCl_4$, and the solution was immediately vortexed for 1 minute. To identify the same particles under optical microscopy and EM, an alpha-numeric reference grid (Ted Pella, Inc.) was patterned on a clean No. 1.5 coverslip (Figure S12). The coverslips were then coated with poly-L-lysine (PLL, 0.01%) to create a positively charged surface. Spherical Au NPs (80-nm, Ted Pella, Inc., 1 pM) – used as additional location markers – and AuNS (1 pM) were drop-cast on the glass.

Differential Interference Contrast Optical Microscopy.

DIC was performed on an inverted Nikon TE2000E with a 100× oil immersion Apo TIRF objective with 1.49 NA, a 1.4 NA oil immersion condenser, and an Andor Zyla 4.2 sCMOS detector. Full lamp power (100 W) was used. The DIC optics included a pair of fixed Nomarski prisms, a de Sénarmont compensator, and an analyzer (Figure 1a, Figure S1). NPs can be visualized under DIC microscopy by incorporating bandpass (BP) filters near the NP resonance.[33-35] We used a 700/10-nm BP filter (Edmund Optics) that was near the ensemble AuNS resonance and within the working range of all optics. DIC images for the correlation study were acquired using exposure times of 0.5 s. Orientation-dependent DIC images were acquired by fixing the glass slide to a round stage ring and manually rotating the ring from α = 0° to 180° in 5° intervals. Z-stacks were acquired for every image, and 80-nm spheres were used to determine the focal plane consistently since their DIC images appear the same at all orientations.

Low-Vacuum Scanning Electron Microscope Imaging and Analysis.

SEM images on non-conductive glass substrates were acquired using low-vacuum mode on an FEI Quanta 600F sFEG ESEM. The large-field gaseous secondary electron detector was used to obtain topographical information from samples, where out-of-plane 3D branches produce brighter contrast. The fit-ellipse algorithm of ImageJ identifies the orientation of arbitrary 2D shapes by defining an ellipse with the same 1st and 2nd image moments,[46-47] and we used this analysis to identify consistently the orientation of arbitrarily shaped AuNS based on SEM images. AuNS volumes were estimated from SEM and TEM images as previously described.[12] AuNS feature sizes (branch length, core diameter, tip radius of curvature) were measured manually from SEM images. Using the patterned alphanumeric grids for reference, the SEM images of each AuNS were aligned corresponding to each DIC image (Figure S12).

Finite-Difference Time-Domain Simulations.

Simulations were performed with commercially available software (FDTD Solutions 2016a, Lumerical Inc.). The AuNS object was designed as a spherical core with conical branches ending in spherical tips with material properties defined by Johnson and Christy.[48] A 2D monitor recorded the full electric and magnetic fields 50 nm above the sample. Results from the 2D monitor were processed with a Lumerical script to generate full DIC images. Additional simulation details are provided in the Supporting Information.

In Situ Gold Nanostar Characterization.

To observe AuNS rotating at the glass-water interface, AuNS (50 pM) in TWEEN-20 (0.01%) were placed in a gasket between a clean No. 1.5 coverslip (no PLL) and the glass slide. Under this condition, single AuNS attached to and rotated on the coverslip without translation or detachment. 300-frame videos were streamed using a 700/10 nm BP filter and exposure times of 0.02-0.5 s. The videos were acquired using the center-quad ROI (1024 × 1024 pixels, 4,430 μm^2) to reduce file size.

Image Processing.

Custom MATLAB programs were written to analyze the DIC image contrast produced by AuNS. The particle intensity, I, was measured as the mean intensity within a round ROI centered on and encompassing the particle image pattern (Figure S6b). The background intensity, I_{bkg}, was the mean intensity within a square ROI that was centered on the particle location but excluded signal from the particle and nearby artifacts (Figure S6c). Local background near each particle was used because intensity gradients occur across DIC images. For the correlation study, contrast data as a function of rotation angle α were fit to $\sin^2(\alpha)$ curve to compare particles quantitatively. $\sin^2(\alpha)$ was chosen for analysis because we expected a sinusoidal behavior of the electric field component parallel to the incident polarization as the particle was rotated, resulting in sine-squared profile for the intensity (i.e. $I \propto E^2$). Since particles were imaged under the same conditions on the same sample, the amplitude (A) of the fit was used to compare the magnitude of the contrast change. The maximum of the fit data corresponded to the substrate rotation angle α at which the brightest DIC contrast was produced. All DIC images of single particles in this manuscript are displayed with I_{bkg} set to the same middle gray value and the same overall intensity range relative to the background.

Supplementary Material

Refer to Web version on PubMed Central for supplementary material.

ACKNOWLEDGMENT

This work was funded by NIH Grant 1R01GM115763. K.S.B.C and A.J.H. were supported by the DoD through the NDSEG fellowship (32 CFR 168a). T.L. was supported by NIH Grant 1R01GM115763. This work made use of the EPIC and BioCryo facilities of Northwestern University NU*ANCE* Center, which has received support from the Soft and Hybrid Nanotechnology Experimental (SHyNE) Resource (NSF ECCS-1542205); the MRSEC program (NSF DMR-1720139) at the Materials Research Center; the International Institute for Nanotechnology (IIN); the Keck Foundation; and the State of Illinois, through the IIN. This work also made use of the NU Biological Imaging Facility. This research was also supported in part through the computational resources and staff contributions

provided for the Quest high performance computing facility at Northwestern University, which is jointly supported by the Office of the Provost, the Office for Research, and Northwestern University Information Technology.

REFERENCES

(1). Li N; Zhao P; Astruc D Anisotropic Gold Nanoparticles: Synthesis, Properties, Applications, and Toxicity. Angew. Chem., Int. Ed. 2014, 53, 1756–1789.

(2). Burda C; Chen X; Narayanan R; El-Sayed MA Chemistry and Properties of Nanocrystals of Different Shapes. Chem. Rev. 2005, 105, 1025–1102. [PubMed: 15826010]

(3). Dreaden EC; Alkilany AM; Huang X; Murphy CJ; El-Sayed MA The Golden Age: Gold Nanoparticles for Biomedicine. Chem. Soc. Rev. 2012, 41, 2740–2779. [PubMed: 22109657]

(4). Murphy CJ; Sau TK; Gole AM; Orendorff CJ; Gao J; Gou L; Hunyadi SE; Li T Anisotropic Metal Nanoparticles: Synthesis, Assembly, and Optical Applications. J. Phys. Chem. B 2005, 109, 13857–13870. [PubMed: 16852739]

(5). Jain PK; Lee KS; El-Sayed IH; El-Sayed MA Calculated Absorption and Scattering Properties of Gold Nanoparticles of Different Size, Shape, and Composition: Applications in Biological Imaging and Biomedicine. J. Phys. Chem. B 2006, 110, 7238–7248. [PubMed: 16599493]

(6). Motl NE; Smith AF; DeSantis CJ; Skrabalak SE Engineering Plasmonic Metal Colloids through Composition and Structural Design. Chem. Soc. Rev. 2014, 43, 3823–3834. [PubMed: 24352187]

(7). Tam F; Moran C; Halas N Geometrical Parameters Controlling Sensitivity of Nanoshell Plasmon Resonances to Changes in Dielectric Environment. J. Phys. Chem. B 2004, 108, 17290–17294.

(8). Webb JA; Erwin WR; Zarick HF; Aufrecht J; Manning HW; Lang MJ; Pint CL; Bardhan R Geometry-Dependent Plasmonic Tunability and Photothermal Characteristics of Multibranched Gold Nanoantennas. J. Phys. Chem. C 2014, 118, 3696–3707.

(9). Chandra K; Culver KSB; Werner SE; Lee RC; Odom TW Manipulating the Anisotropic Structure of Gold Nanostars Using Good's Buffers. Chem. Mater. 2016, 28, 6763–6769.

(10). Walker DA; Leitsch EK; Nap RJ; Szleifer I; Grzybowski BA Geometric Curvature Controls the Chemical Patchiness and Self-Assembly of Nanoparticles. Nat. Nanotechnol. 2013, 8, 676–681. [PubMed: 23955810]

(11). Rotz MW; Culver KSB; Parigi G; MacRenaris KW; Luchinat C; Odom TW; Meade TJ High Relaxivity Gd(III)–DNA Gold Nanostars: Investigation of Shape Effects on Proton Relaxation. ACS Nano 2015, 9, 3385–3396. [PubMed: 25723190]

(12). Culver KSB; Shin YJ; Rotz MW; Meade TJ; Hersam MC; Odom TW Shape-Dependent Relaxivity of Nanoparticle-Based T1 Magnetic Resonance Imaging Contrast Agents. J. Phys. Chem. C 2016, 120, 22103–22109.

(13). Zeng J; Zhang Q; Chen J; Xia Y A Comparison Study of the Catalytic Properties of Au-Based Nanocages, Nanoboxes, and Nanoparticles. Nano Lett. 2010, 10, 30–35. [PubMed: 19928909]

(14). Soetan N; Zarick HF; Banks C; Webb JA; Libson G; Coppola A; Bardhan R Morphology-Directed Catalysis with Branched Gold Nanoantennas. J. Phys. Chem. C 2016, 120, 10320–10327.

(15). Xie JP; Lee JY; Wang DIC Seedless, Surfactantless, High-Yield Synthesis of Branched Gold Nanocrystals in HEPES Buffer Solution. Chem. Mater. 2007, 19, 2823–2830.

(16). Dam DHM; Lee JH; Sisco PN; Co DT; Zhang M; Wasielewski MR; Odom TW Direct Observation of Nanoparticle–Cancer Cell Nucleus Interactions. ACS Nano 2012, 6, 3318–3326. [PubMed: 22424173]

(17). Dam DHM; Culver KSB; Odom TW Grafting Aptamers onto Gold Nanostars Increases in Vitro Efficacy in a Wide Range of Cancer Cell Types. Mol. Pharmaceutics 2014, 11, 580–587.

(18). Lee H; Dam DHM; Ha JW; Yue J; Odom TW Enhanced Human Epidermal Growth Factor Receptor 2 Degradation in Breast Cancer Cells by Lysosome-Targeting Gold Nanoconstructs. ACS Nano 2015, 9, 9859–9867. [PubMed: 26335372]

(19). Chen H; Zhang X; Dai S; Ma Y; Cui S; Achilefu S; Gu Y Multifunctional Gold Nanostar Conjugates for Tumor Imaging and Combined Photothermal and Chemo-Therapy. Theranostics 2013, 3, 633–649. [PubMed: 24019851]

(20). Saverot S; Geng X; Leng W; Vikesland PJ; Grove TZ; Bickford LR Facile, Tunable, and SERS-Enhanced HEPES Gold Nanostars. RSC Adv. 2016, 6, 29669–29673.

(21). Moser TH; Mehta H; Park C; Kelly RT; Shokuhfar T; Evans JE The Role of Electron Irradiation History in Liquid Cell Transmission Electron Microscopy. Science Advances 2018, DOI: 10.1126/sciadv.aaq1202.

(22). Sagle LB; Ruvuna LK; Bingham JM; Liu C; Cremer PS; Van Duyne RP Single Plasmonic Nanoparticle Tracking Studies of Solid Supported Bilayers with Ganglioside Lipids. J. Am. Chem. Soc. 2012, 134, 15832–15839. [PubMed: 22938041]

(23). Gu Y; Di X; Sun W; Wang G; Fang N Three-Dimensional Super-Localization and Tracking of Single Gold Nanoparticles in Cells. Anal. Chem. 2012, 84, 4111–4117. [PubMed: 22458652]

(24). Sonnichsen C; Alivisatos AP Gold Nanorods as Novel Nonbleaching Plasmon-Based Orientation Sensors for Polarized Single-Particle Microscopy. Nano Lett. 2005, 5, 301–304. [PubMed: 15794615]

(25). Chaudhari K; Pradeep T Spatiotemporal Mapping of Three Dimensional Rotational Dynamics of Single Ultrasmall Gold Nanorods. Sci. Rep. 2014, 4, 5948. [PubMed: 25091698]

(26). Ishmukhametov R; Hornung T; Spetzler D; Frasch WD Direct Observation of Stepped Proteolipid Ring Rotation in E. Coli FoF1-ATP Synthase. EMBO J. 2010, 29, 3911–3923. [PubMed: 21037553]

(27). Gu Y; Sun W; Wang G; Fang N Single Particle Orientation and Rotation Tracking Discloses Distinctive Rotational Dynamics of Drug Delivery Vectors on Live Cell Membranes. J. Am. Chem. Soc. 2011, 133, 5720–5723. [PubMed: 21438558]

(28). Gu Y; Sun W; Wang G; Jeftinija K; Jeftinija S; Fang N Rotational Dynamics of Cargos at Pauses During Axonal Transport. Nat. Commun. 2012, 3, 1030. [PubMed: 22929787]

(29). Xu D; He Y; Yeung ES Direct Observation of the Orientation Dynamics of Single Protein - Coated Nanoparticles at Liquid/Solid Interfaces. Angew. Chem., Int. Ed. 2014, 126, 7071–7075.

(30). Wang G; Sun W; Luo Y; Fang N Resolving Rotational Motions of Nano-Objects in Engineered Environments and Live Cells with Gold Nanorods and Differential Interference Contrast Microscopy. J. Am. Chem. Soc. 2010, 132, 16417–16422. [PubMed: 21043495]

(31). Sweeney CM; Nehl CL; Hasan W; Liang T; Eckermann AL; Meade TJ; Odom TW Three-Channel Spectrometer for Wide-Field Imaging of Anisotropic Plasmonic Nanoparticles. J. Phys. Chem. C 2011, 115, 15933–15937.

(32). van Dijk MA; Tchebotareva AL; Orrit M; Lippitz M; Berciaud S; Lasne D; Cognet L; Lounis B Absorption and Scattering Microscopy of Single Metal Nanoparticles. Phys. Chem. Chem. Phys. 2006, 8, 3486–3495. [PubMed: 16871337]

(33). Luo Y; Sun W; Gu Y; Wang G; Fang N Wavelength-Dependent Differential Interference Contrast Microscopy: Multiplexing Detection Using Nonfluorescent Nanoparticles. Anal. Chem. 2010, 82, 6675–6679. [PubMed: 20614872]

(34). Sun W; Wang G; Fang N; Yeung ES Wavelength-Dependent Differential Interference Contrast Microscopy: Selectively Imaging Nanoparticle Probes in Live Cells. Anal. Chem. 2009, 81, 9203–9208. [PubMed: 19788254]

(35). Ha JW; Sun W; Stender AS; Fang N Dual-Wavelength Detection of Rotational Diffusion of Single Anisotropic Nanocarriers on Live Cell Membranes. J. Phys. Chem. C 2012, 116, 2766–2771.

(36). Habib A; Tabata M; Wu YG Formation of Gold Nanoparticles by Good's Buffers. Bull. Chem. Soc. Jpn. 2005, 78, 262–269.

(37). Liu H; Xu Y; Qin Y; Sanderson W; Crowley D; Turner CH; Bao Y Ligand-Directed Formation of Gold Tetrapod Nanostructures. J. Phys. Chem. C 2013, 117, 17143–17150.

(38). Xiao L; Ha JW; Wei L; Wang G; Fang N Determining the Full Three-Dimensional Orientation of Single Anisotropic Nanoparticles by Differential Interference Contrast Microscopy. Angew. Chem., Int. Ed. 2012, 51, 7734–7738.

(39). Stender AS; Wang G; Sun W; Fang N Influence of Gold Nanorod Geometry on Optical Response. ACS Nano 2010, 4, 7667–7675. [PubMed: 21090741]

(40). Hu J; Liu C-H; Ren X; Lauhon LJ; Odom TW Plasmonic Lattice Lenses for Multiwavelength Achromatic Focusing. ACS Nano 2016, 10, 10275–10282. [PubMed: 27786448]

(41). Suh JY; Odom TW Nonlinear Properties of Nanoscale Antennas. Nano Today 2013, 8, 469–479.

(42). Kildishev AV; Boltasseva A; Shalaev VM Planar Photonics with Metasurfaces. Science 2013, 339, 1232009. [PubMed: 23493714]

(43). Kim JY; Lim J; Jin HM; Kim BH; Jeong S-J; Choi DS; Li DJ; Kim SO 3d Tailored Crumpling of Block-Copolymer Lithography on Chemically Modified Graphene. Adv. Mater. 2016, 28, 1591–1596. [PubMed: 26660004]

(44). Son JG; Gotrik KW; Ross CA High-Aspect-Ratio Perpendicular Orientation of PS-b-PDMS Thin Films under Solvent Annealing. ACS Macro Lett. 2012, 1, 1279–1284.

(45). Yue J; Feliciano TJ; Li W; Lee A; Odom TW Gold Nanoparticle Size and Shape Effects on Cellular Uptake and Intracellular Distribution of siRNA Nanoconstructs. Bioconjugate Chem. 2017, 28, 1791–1800.

(46). Teague MR Image Analysis Via the General Theory of Moments. J. Opt. Soc. Am. 1980, 70, 920–930.

(47). Mulchrone KF; Choudhury KR Fitting an Ellipse to an Arbitrary Shape: Implications for Strain Analysis. J. Struct. Geol 2004, 26, 143–153.

(48). Johnson PB; Christy RW Optical Constants of the Noble Metals. Phys. Rev. B 1972, 6, 4370–4379.

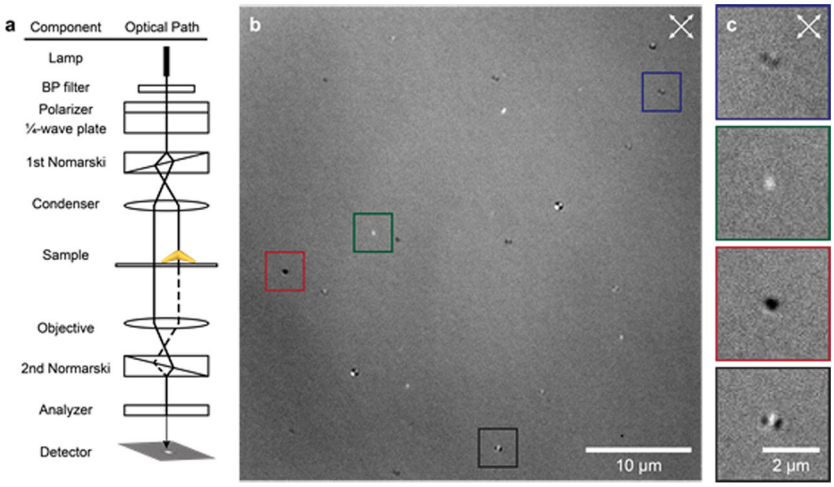

Figure 1. Wide-field DIC microscopy of AuNS.

(a) Scheme of DIC optical components and light path. **(b)** Wide-field DIC image of AuNS dispersed on the coverslip. **(c)** Zoomed-in DIC images of particles in colored squares highlight the distinct patterns produced by different AuNS. White arrows indicate the polarizations of the ordinary and extraordinary beams.

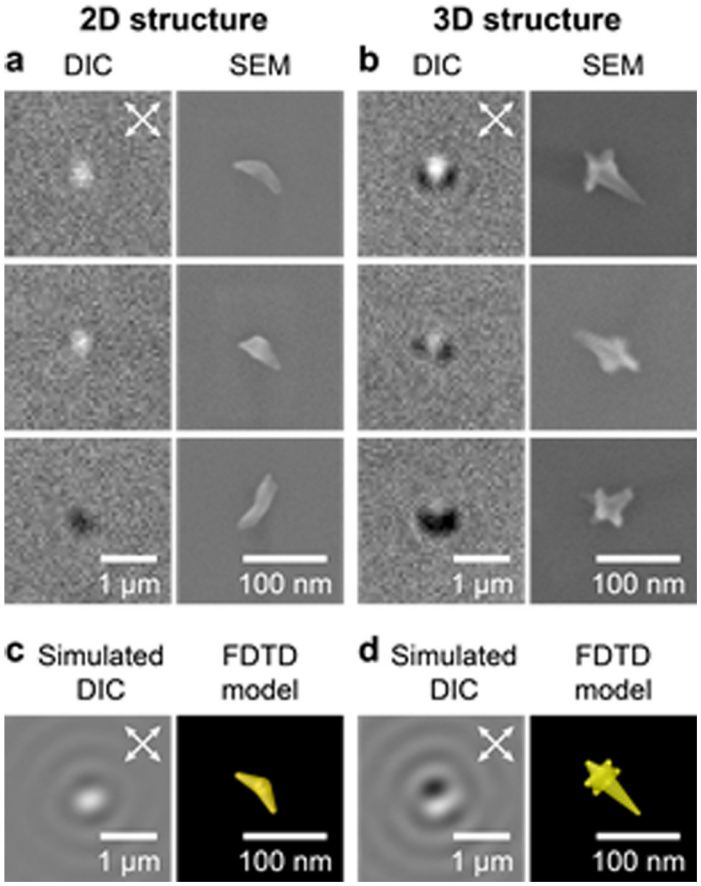

Figure 2. DIC image patterns distinguish between 2D and 3D AuNS geometries.

Correlated SEM and DIC images of **(a)** 2D AuNS showing plain bright or dark DIC image patterns and **(b)** 3D AuNS showing lobed DIC image patterns. **(c)** Simulated DIC images and structure of a 2D AuNS. **(d)** Simulated DIC images and structure of a 3D AuNS.

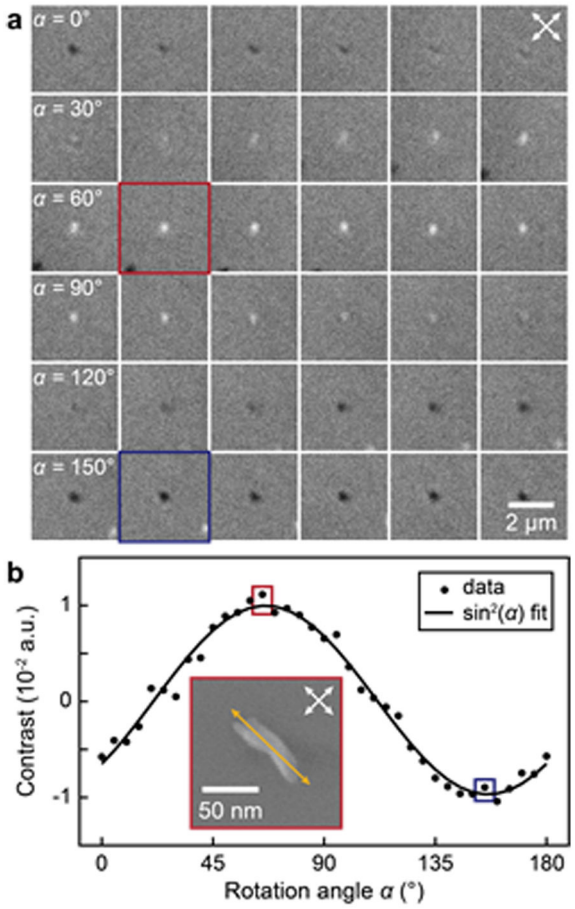

Figure 3. DIC contrast can be used to identify AuNS orientation.

(a) DIC images taken from a full 0° to 180° stage rotation of a 2D AuNS. White arrows indicate the polarization of the ordinary and extraordinary beams. **(b)** Quantified DIC contrast (circles) and the fit to a $\sin^2(\alpha)$ equation (black line). Inset is the SEM image of the particle aligned to the maximum contrast (α = 65°, red box). The yellow arrow is the particle orientation (θ = 136°) as determined from fit ellipse analysis of the SEM image.

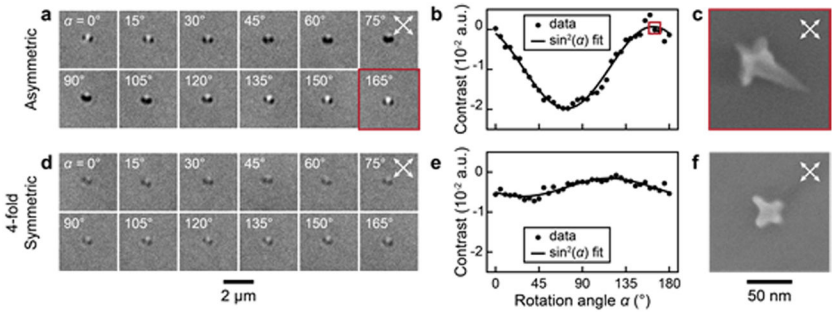

Figure 4. Orientation-dependent DIC of asymmetric and symmetric 3D AuNS.

(a) DIC images at different orientations, **(b)** contrast with fit, and **(c)** SEM image of an asymmetric 3D AuNS. **(d)** DIC images and **(e)** contrast with fit show weak orientation-dependence for a AuNS with nearly 4-fould symmetry **(f)**.

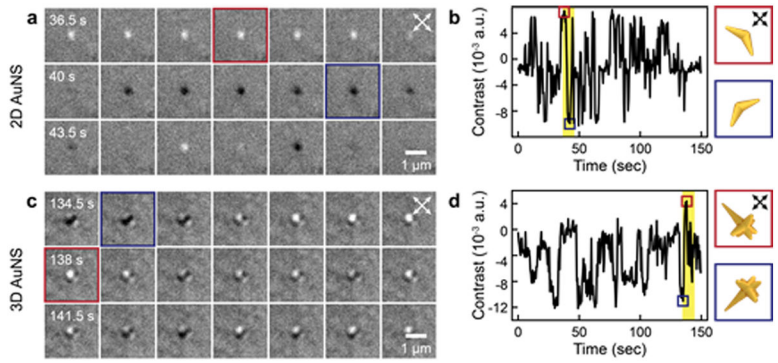

Figure 5. Identification of 2D or 3D geometry and orientation of two different AuNS rotating at a glass-water interface.

(a) Non-lobed image patterns indicate a 2D structure. **(b)** Quantified contrast was used to track orientation of the 2D AuNS. **(c)** Lobed image patterns indicate a 3D geometry. **(d)** Quantified contrast was used to track orientation of the 3D AuNS. The regions highlighted in yellow correspond to the 21 consecutive frames shown in **(a)** and **(c)**. The red and blue boxes indicate the frames with brightest and darkest contrast that correspond to alignment with the polarization of the extraordinary and ordinary beams, respectively.